A Nested Domain Decomposition Method for Simulations of Resistivity Borehole Micro-imaging Tool

Jiefu Chen

Advantage R&D Center, Weatherford, 16210 W Hardy Rd., Houston, TX 77060, USA. jiefu.chen@weatherford.com

Abstract

A nested domain decomposition method is proposed to study the responses of resistivity borehole micro-imaging tools used in the oil and gas exploration industry. The multiscale structure of an imaging problem is decomposed into several nested subdomains based on its geometric characteristics. Each subdomain is discretized independently, and numerical flux is used to couple all subdomains together. The nested domain decomposition scheme will lead to a block tridiagonal linear system, and the block Thomas algorithm is utilized here to eliminate the subdomain based iteration in the step of solving the linear system. Numerical results demonstrate the validity and efficiency of this method.

1. Introduction

Resistivity borehole micro-imaging tools [1] are very useful in oilfield services. As shown in the left panel of Fig. 1, by providing high definition images of borehole wall resistivity distribution, micro-imaging tools unveil detailed subsurface structures such as fractures, vugs, bed interfaces, faults, etc., which are very important in oil and gas drilling and production. Modeling resistivity micro-imaging is oftentimes a multiscale problem. As shown in the right panel of Fig. 1, the length of an imaging tool is several meters, while the details in the imaging sensor and the fractures on the borehole wall can be as small as a few millimeters. This multiscale property will raise big challenges for conventional numerical methods. In this study we employ the discontinuous Galerkin finite element method (DG-FEM) [2] with nested domain decomposition to solve this multiscale problem. The whole structure is divided into several subdomains in a nested way: small and lower order finite elements are used to capture geometric characteristics of fine structures such as imaging sensors and fractures on the borehole wall; large and higher order finite elements are used to efficiently discretize electrically coarse structures. Subdomains are discretized independently. The numerical flux is utilized to stitch all subdomain together. A nested domain decomposition will lead to a block tridiagonal linear system, and can use the block Thomas method [3], an iteration free algorithm, to solve the system of matrix equations with a high efficiency.

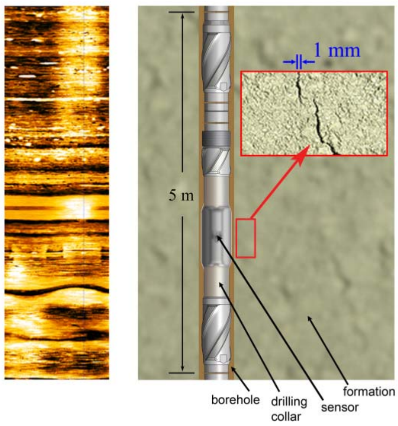

Fig. 1. Left: a typical resistivity borehole image with recognizable patterns of fractures, vugs, bed interfaces, etc.; Right: Schematic of a resistivity micro-imaging tool in formation with fine details.

2. Formulations

For micro-imaging tools working in water based mud, the Galerkin's weak forms with current density $\boldsymbol{J}$ and electric potential Φ as variables are

$$\iiint_V \nabla N_\Phi \cdot \boldsymbol{J} dV - \iint_S N_\Phi \hat{\boldsymbol{n}} \cdot \boldsymbol{J} dS = 0 \tag{1}$$

$$\iiint_V \boldsymbol{N}_J \cdot \boldsymbol{J} dV - \iiint_V (\sigma + j\omega\varepsilon)(\nabla \cdot \boldsymbol{N}_J)\Phi dV + \iint_S (\sigma + j\omega\varepsilon)(\hat{\boldsymbol{n}} \cdot \boldsymbol{N}_J)\Phi dS = \iiint_V \boldsymbol{N}_J \cdot \boldsymbol{J}_e dV \tag{2}$$

where ω is working frequency of the imaging tool, $\boldsymbol{J}_e$ is the external current density. ε is materials permittivity, and σ denotes conductivity, which is the inverse of electrical resistivity. N_Φ and $\boldsymbol{N}_J$ are basis function for Φ and $\boldsymbol{J}$, respectively.

978-1-4673-5225-3/14/$31.00 ©2014 IEEE

V and S denote volume and surface, respectively. $\hat{\boldsymbol{n}}$ is unit normal vector located on S pointing to the outside of V. The surface integration items in (1) and (2) are determined by either boundary conditions (for boundaries) or numerical fluxes (for interfaces between subdomains). Assuming the k-th and the l-th subdomains as the local subdomain and its neighbor, respectively, the interface evaluations of $\hat{\boldsymbol{n}} \cdot \boldsymbol{J}$ and Φ are determined by the field values of subdomains on both sides

$$\hat{\boldsymbol{n}} \cdot \boldsymbol{J} = \left(\hat{\boldsymbol{n}} \cdot \boldsymbol{J}^{(k)} + \hat{\boldsymbol{n}} \cdot \boldsymbol{J}^{(l)}\right)/2 + C_{11}\left(\hat{\boldsymbol{n}} \cdot \boldsymbol{J}^{(k)} - \hat{\boldsymbol{n}} \cdot \boldsymbol{J}^{(l)}\right) + C_{12}\left(\Phi^{(k)} - \Phi^{(l)}\right) \tag{3}$$

$$\Phi = \left(\Phi^{(k)} + \Phi^{(l)}\right)/2 + C_{21}\left(\hat{\boldsymbol{n}} \cdot \boldsymbol{J}^{(k)} - \hat{\boldsymbol{n}} \cdot \boldsymbol{J}^{(l)}\right) + C_{22}\left(\Phi^{(k)} - \Phi^{(l)}\right) \tag{4}$$

where coefficients C_{11}, C_{12}, C_{21}, and C_{22} can have different choices [4]. In the following two examples we set the coefficients as $C_{11} = -0.5$, $C_{12} = -4$, $C_{21} = 0$, and $C_{22} = 0.5$, which are corresponding to an upwind flux.

Assuming a micro-imaging problem is divided into N subdomains, the discretized equations by DG-FEM are

$$\boldsymbol{K}_{\Phi J}^{(k)} \boldsymbol{j}^{(k)} + \sum_{l=1}^{N}\left(\boldsymbol{L}_{\Phi\Phi}^{(kl)} \boldsymbol{\varphi}^{(l)} + \boldsymbol{L}_{\Phi J}^{(kl)} \boldsymbol{j}^{(l)}\right) = \boldsymbol{0} \tag{5}$$

$$\boldsymbol{M}_{JJ}^{(k)} \boldsymbol{j}^{(k)} + \boldsymbol{K}_{J\Phi}^{(k)} \boldsymbol{\varphi}^{(k)} + \sum_{l=1}^{N}\left(\boldsymbol{L}_{J\Phi}^{(kl)} \boldsymbol{\varphi}^{(l)} + \boldsymbol{L}_{JJ}^{(kl)} \boldsymbol{j}^{(l)}\right) = \boldsymbol{j}_{e}^{(k)} \tag{6}$$

where $k = 1,2,\cdots,N$. $\boldsymbol{\varphi}^{(k)}$ and $\boldsymbol{j}^{(k)}$ are vectors of the discretized electric potential and current density, and $\boldsymbol{j}_e^{(k)}$ is vector of discretized external excitation. $\boldsymbol{M}_{JJ}^{(k)}$, $\boldsymbol{K}_{\Phi J}^{(k)}$, and $\boldsymbol{K}_{J\Phi}^{(k)}$ are mass and stiffness matrices of the k-th subdomain. Matrices $\boldsymbol{L}_{\Phi\Phi}^{(kl)}$, $\boldsymbol{L}_{\Phi J}^{(kl)}$, $\boldsymbol{L}_{J\Phi}^{(kl)}$, and $\boldsymbol{L}_{JJ}^{(kl)}$ are obtained from the interface integrations and can be viewed as the couplings between fields of the k-th and l-th subdomain. Detailed formulations of the above matrices are referred to [5].

For the sake of simplicity we rewrite the discretized system (5) and (6) as

$$\boldsymbol{K}^{(k)} \boldsymbol{v}^{(k)} + \sum_{l=1}^{N} \boldsymbol{L}^{(kl)} \boldsymbol{v}^{(l)} = \boldsymbol{f}^{(k)}, \quad k = 1,2,\cdots,N \tag{7}$$

where

$$\boldsymbol{K}^{(k)} = \begin{bmatrix} \boldsymbol{0} & \boldsymbol{K}_{\Phi J}^{(k)} \\ \boldsymbol{K}_{J\Phi}^{(k)} & \boldsymbol{M}_{JJ}^{(k)} \end{bmatrix}, \quad \boldsymbol{L}^{(kl)} = \begin{bmatrix} \boldsymbol{L}_{\Phi\Phi}^{(kl)} & \boldsymbol{L}_{\Phi J}^{(kl)} \\ \boldsymbol{L}_{J\Phi}^{(kl)} & \boldsymbol{L}_{JJ}^{(kl)} \end{bmatrix}, \quad \boldsymbol{v}^{(k)} = \begin{Bmatrix} \boldsymbol{\varphi}^{(k)} \\ \boldsymbol{j}^{(k)} \end{Bmatrix}, \quad \boldsymbol{f}^{(k)} = \begin{Bmatrix} \boldsymbol{0} \\ \boldsymbol{j}_e^{(k)} \end{Bmatrix} \tag{8}$$

The discretized DG-FEM system (7) can be solved by subdomain based iterative algorithms, such as the Block Gauss-Seidel method. However, an iterative algorithm can become quite slow if the convergence threshold is set as a very small value, or if the problem has many subdomains. Here we propose a nested domain decomposition strategy to efficiently discretize the multiscale imaging problem as shown in Fig. 2, and we can see that the coupling between subdomains by the nested decomposition can be described as in a serial way, i.e. subdomain SD1 is coupled with SD2, SD2 coupled with SD1 and SD3, SD3 coupled with SD2 and SD4, and so forth. This serial coupling will lead to a block tridiagonal pattern of the system matrix equations, as shown in the right panel of Fig. 2.

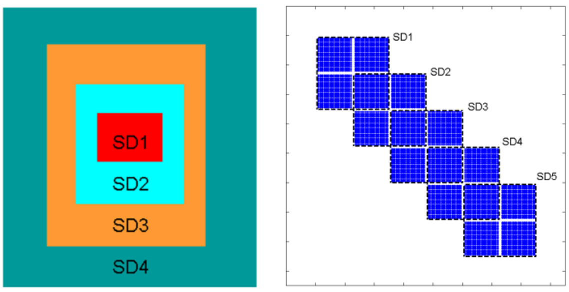

Fig. 2. Left: schematic of a nested domain decomposition; Right: matrix pattern of a block tridiagonal system by the nested domain decomposition.

For a block tridiagonal DG-FEM system, $\boldsymbol{L}^{(kl)} = \boldsymbol{0}$ when $|k-l| \geq 2$, and it can be efficiently solved by the block Thomas method [3]. From the steps of the block Thomas method shown in (9) we can see that this algorithm is free of iteration controlled by convergence threshold. In other words, solving the tridiagonal DG-FEM discretized system can be performed in a deterministic number of steps of calculation, instead of being determined by whether or not meeting the convergence condition. This iteration-free scheme will not have nonconvergence issue under any circumstance.

$$
\begin{aligned}
&\boldsymbol{A}_k = \boldsymbol{L}^{(k,k-1)}, \boldsymbol{B}_k = \boldsymbol{K}^{(k)} + \boldsymbol{L}^{(k,k)}, \boldsymbol{C}_k = \boldsymbol{L}^{(k,k+1)}\\
&\textbf{solve}\quad \boldsymbol{B}_1\widetilde{\boldsymbol{C}}_1 = \boldsymbol{C}_1\\
&\textbf{for}\quad k = 2{:}\,N-1,\ \ \textbf{do}\\
&\quad \widetilde{\boldsymbol{B}}_k = \boldsymbol{B}_k - \boldsymbol{A}_k\widetilde{\boldsymbol{C}}_{k-1},\ \ \textbf{solve}\quad \widetilde{\boldsymbol{B}}_k\widetilde{\boldsymbol{C}}_k = \boldsymbol{C}_k\\
&\textbf{end for}\\
&\textbf{solve}\quad \boldsymbol{B}_1\tilde{\boldsymbol{f}}^{(1)} = \boldsymbol{f}^{(1)}\\
&\textbf{for}\quad k = 2{:}\,N,\ \ \textbf{do}\\
&\quad \textbf{solve}\quad \widetilde{\boldsymbol{B}}_k\tilde{\boldsymbol{f}}^{(k)} = \boldsymbol{f}^{(k)} - \boldsymbol{A}_k\tilde{\boldsymbol{f}}^{(k-1)}\\
&\textbf{end for}\\
&\boldsymbol{v}^{(N)} = \tilde{\boldsymbol{f}}^{(N)}\\
&\textbf{for}\quad k = N-1{:}-1{:}\,1,\ \ \textbf{do}\\
&\quad \boldsymbol{v}^{(k)} = \tilde{\boldsymbol{f}}^{(k)} - \widetilde{\boldsymbol{C}}_k\boldsymbol{v}^{(k+1)}\\
&\textbf{end for}
\end{aligned}
\tag{9}
$$

3. Results and Discussions

The left panel of Fig. 3 shows a micro-imaging tool sitting in the center of a borehole, with homogeneous and infinitely large formation as background medium. The voltage of imaging sensor is set as 1 V, and the working frequency used here is 100 KHz. We first assume there is no borehole; under this circumstance the measured current by imaging sensor should be inversely proportional to the formation resistivity. We solve this problem by the conventional FEM and the proposed DG-FEM. Numerical results shown in the center panel of Fig. 3 prove the inverse proportionality between sensor signal and formation resistivity, and also demonstrate the excellent agreement between FEM and DG-FEM. We then set the standoff between tool and borehole wall as 0.5 inch, and assume the borehole is filled with 0.1 ohm-m conductive mud. Sensor currents w.r.t. to formation resistivity are shown in the right panel of Fig. 3, from which we can see that the relationship between sensor current and formation resistivity is no longer a simple straight line in a log-log scale plot. The two saturation stages (the two flat ends) are due to the existence of borehole and mud resistivity, and further studies shows they will become longer (thus decrease the linear range of the tool) when standoff increases.

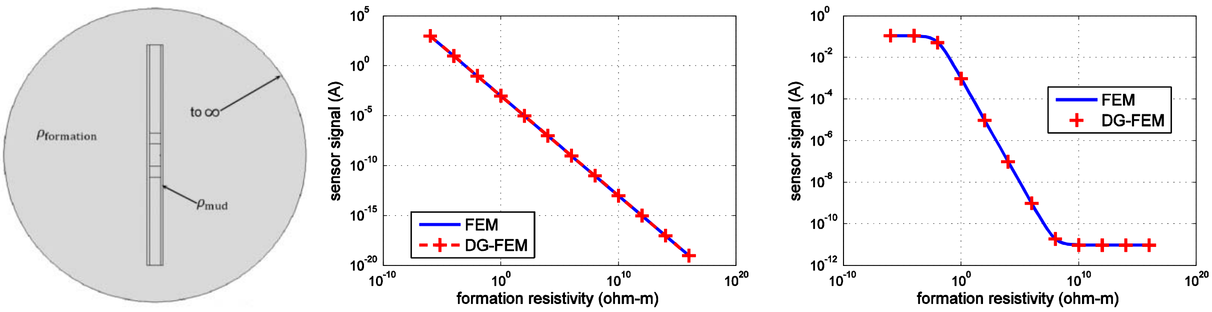

Fig. 3. Left: a miro-imaging tool centered in borehole; the background medium is homogeneous and infinitely large formation. Middle: current w.r.t. formation resistivity. Borehole does not exist in this case. Right: current w.r.t. formation resistivity. Standoff is 0.5 inch, and mud resistivity is 0.1 ohm-m.

The second case is shown in Fig. 4: a tank is filled with 0.2 ohm-m salty water, where a block of 3.7 ohm-m formation is submerged. A groove is made at the top of block to host the imaging tool, and several slices with different thicknesses are carved out along different directions in the groove. Fig. 5 shows the current curves when the sensor moves across a 0.06 inch thick fracture and a 0.5 inch thick fracture by measurement and two numerical methods. Tab. 1 lists the imaging sensor resolution evaluated by the full width at half maximum (FWHM) for the two fractures, from which good agreements are observed among all the three methods.

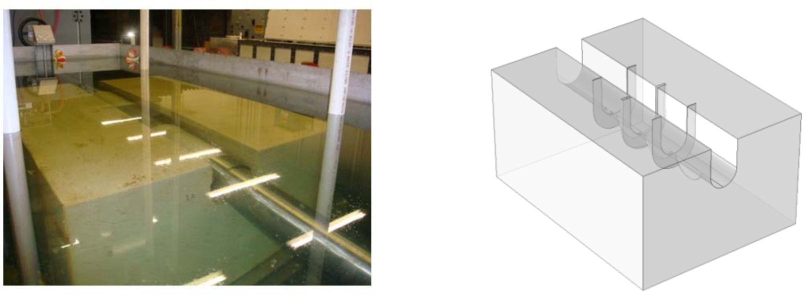

Fig. 4. Left: a photo of the tank test; Right: the block submerged in water, with fractures along different directions in its groove.

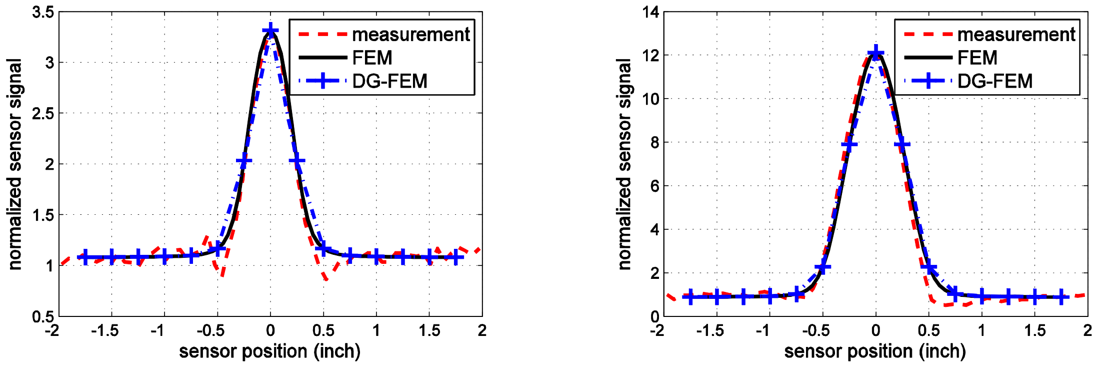

Fig. 5. Left: the current curves when the sensor moves across a 0.06 inch thick fracture; Right: the current curves when the sensor moves across a 0.5 inch thick fracture.

Tab. 1. FWHM of the two fractures by measurement and by simulations

	measurement	FEM	DG-FEM
0.06 inch fracture	0.44 inch	0.46 inch	0.46 inch
0.5 inch fracture	0.61 inch	0.60 inch	0.60 inch

Fig. 6 shows 220-pixel-by-128-pixel images of the tank test by measurement and by the DG-FEM. We can see that these two images agree with each other every well. In a full image simulation, each pixel is corresponding to an independent simulation, and each one requires its own meshing, matrix assembling, and system solving if the conventional FEM is used. On the other hand, the DG-FEM only needs to work on the center submain containing the imaging sensor for different pixel. The efforts of generating meshing, assembling and factorizing system matrices of all the other subdomains can be calculated at the beginning, then stored and used throughout the simulation. This strategy will save a big amount of computational cost in a full image simulation by DG-FEM. Tab. 2 lists the computational time by the two methods, from which we observe that the DG-FEM is much more efficient than the conventional FEM.

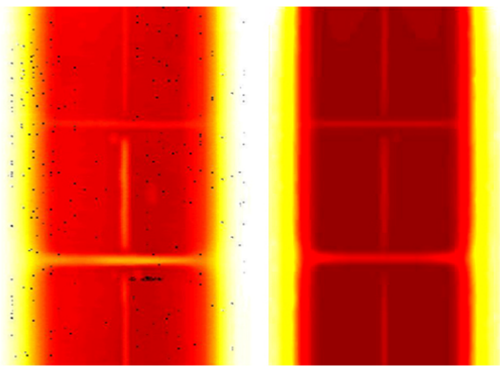

Fig. 6. Left: a measured image of the tank test; Right: a simulated image by DG-FEM.

Tab. 2. Computational time of the tank case

	FEM	DG-FEM
CPU time	91.7 hours	16.7 hours

4. Conclusion

A DG-FEM with nested domain decomposition is proposed in this paper. Numerical results show that this method is more efficient than conventional FEM in modeling multiscale micro-imaging problems.

References

[1] S. Luthi, *Geological Well Logs: Their Use in Reservoir Modeling*, Springer, 2001.
[2] J. S. Hesthaven, and T. Warburton, *Nodal Discontinuous Galerkin Method*, Springer, 2008.
[3] G. Meurant, "A Review on the Inverse of Symmetric Tridiagonal and Block Tridiagonal Matrices," *SIAM J Matrix Anal. Appl.*, 1992, pp. 707-728.
[4] B. Q. Li, *Discontinuous Finite Elements in Fluid Dynamics and Heat Transfer*, Springer, 2006.
[5] J. Chen, and Q. H. Liu, "Discontinuous Galerkin Time-Domain Methods for Multiscale Electromagnetic Simulations: A Review," *Proc. IEEE*, 2013, 242-254.